Electronic Supplementary Material (ESI) for Nanoscale Horizons.
This journal is © The Royal Society of Chemistry 2024

Supplementary Information: Pentagonal nanowires from topological crystalline insulators: a platform for intrinsic core-shell nanowires and higher-order topology

Ghulam Hussain,[1,2] Giuseppe Cuono,[2,3] Piotr Dziawa,[4] Dorota Janaszko,[4] Janusz Sadowski,[4] Slawomir Kret,[4] Bogusława Kurowska,[4] Jakub Polaczyński,[2] Kinga Warda,[2,5] Shahid Sattar,[6] Carlo M. Canali,[6] Alexander Lau,[2] Wojciech Brzezicki,[2] Tomasz Story,[2,4] and Carmine Autieri[2,*]

[1] *Institute for Advanced Study, Shenzhen University, Shenzhen 518060, China*
[2] *International Research Centre MagTop, Institute of Physics, Polish Academy of Sciences, Aleja Lotników 32/46, PL-02668 Warsaw, Poland*
[3] *Consiglio Nazionale delle Ricerche (CNR-SPIN), Unitá di Ricerca presso Terzi c/o Universitá "G. D'Annunzio", 66100 Chieti, Italy*
[4] *Institute of Physics, Polish Academy of Sciences, Aleja Lotników 32/46, PL-02668 Warsaw, Poland*
[5] *Faculty of Applied Physics and Mathematics, Gdansk University of Technology, Gdańsk 80-233, Poland*
[6] *Department of Physics and Electrical Engineering, Linnaeus University, 392 31 Kalmar, Sweden*

(Dated: May 15, 2024)

We report on the experimental realization of $Pb_{1-x}Sn_xTe$ pentagonal nanowires (NWs) with [110] orientation using molecular beam epitaxy techniques. Using first-principles calculations, we investigate the structural stability in NWs of SnTe and PbTe in three different structural phases: cubic, pentagonal with [001] orientation and pentagonal with [110] orientation. Within a semiclassical approach, we show that the interplay between ionic and covalent bonds favors the formation of pentagonal NWs. Additionally, we find that this pentagonal structure is more likely to occur in tellurides than in selenides. The disclination and twin boundary cause the electronic states originating from the NW core region to generate a conducting band connecting the valence and conduction bands, creating a symmetry-enforced metallic phase. The metallic core band has opposite slopes in the cases of Sn and Te twin boundary, while the bands from the shell are insulating. We finally study the electronic and topological properties of pentagonal NWs unveiling their potential as a new platform for higher-order topology and fractional charge. These pentagonal NWs represent a unique case of intrinsic core-shell one-dimensional nanostructures with distinct structural, electronic and topological properties between the core and the shell region.

Appendix A: Experimental setup

$Pb_{1-x}Sn_xTe$ NWs were grown by molecular beam epitaxy technique in a home-built system equipped with SnTe, Pb and Te solid sources. We used commercial (Azelis, France) both (100)- and (111)-oriented p-Si substrates covered with a relatively thin oxide layer (up to 10 Å) such that we observed slight streaky reflection high-energy electron diffraction (RHEED) patterns even without any surface preparation. Covering the surface with an amorphous SiO_x layer prevents deposition directly on monocrystalline silicon. On the other hand, these oxides support the mobility of the adatoms on the surface. To uncover Si, the etching procedure in HF was employed. Different solutions of acid (from 8% to 40%), as well as various times of etching (up to 2 min), were applied resulting in different oxides covering stages. The aim was to achieve separated pinholes in oxide which can play the role of the base for the nucleation center. Before loading into load-lock the freshly etched Si substrates were kept in ethanol to protect them against the air. Instead of the typically exploited vapor-liquid-solid (VLS) mode of growth effective for IV-VI, e.g. using Au nanodroplets as a catalyst[1], we applied vapor-solid (VS) mode. The growth temperature was in the range from 450 °C to 500 °C. The SnTe/Pb molecular beam flux ratio was kept to obtain $x \approx 0.50 \pm 0.05$ in $Pb_{1-x}Sn_xTe$. The total molecular flux used to grow NWs corresponds to the rate of growth for layers from 0.1 Å/s to 0.2 Å/s. This results in NWs longer than 1 μm and the rate of NWs growth higher than 0.5 μm/h. Diameters of the NWs show relatively wide distribution from the smallest around 15 nm to even 200 nm with the maximum at approximately 40-80 nm. Under these conditions both types of NWs are observed, i.e., exhibiting four-fold and five-fold symmetry of cross-section (see Fig. **??**a).

SEM observations were made using Scanning Electron Microscope ZEISS Auriga - CrossBeam Workstation, images were made at 5 kV with magnification from 10k to 300k x. The images show that the length of the NWs varies from 0.7 μm to 3 μm, and the width of the structures ranges between 40-150 nm. The surface density is from 0.1 to even 5 μm^{-1}. On the substrate, we observed five-fold NWs with greater amounts, less often four-fold NWs. Structures are symmetrical and well-shaped with visible blocks. The surface of the NWs was smooth without any imperfections. Structural properties of the $Pb_{1-x}Sn_xTe$ NWs were examined using FEI-Titan 80-300 transmission electron microscope operating at 300 kV, equipped with an image corrector and HAADF scanning transmission electron microscopy detector. The cross-sectioned NWs were prepared with the Thermo Scientific's Helios G1 NanoLab DualBeam 600 Scanning Electron Microscope, with FIB (Focused Ion

Beam)- resolution of 5.0 nm at 30 kV, and lift-off procedure for cross-sections with an Omni-Probe nanomanipulator. The cross-sectioned NWs were investigated in the zone axis [110] which is parallel to the NWs growth axis, in scanning transmission electron microscopy as well as in high-resolution transmission electron microscopy mode. The five-fold symmetry was confirmed, and the (111) planes twin boundaries were visible as well as brighter areas on the twin. These areas are related to strain fields that are visible to distinguish for observations under camera length 0.230 m. EDS determined the averaged elemental ratio as Sn:Pb = 55:45 (∼1:1).

The pentagonal NWs grow directly on both the substrate and the crystallites. The occurrence of pentagonal NWs is observed regardless of the substrate orientation Si(100) or Si(111). Therefore, the growth of pentagonal nanowires appears in a relatively broad range of growth conditions.

The crystal structure can be switched from cubic to pentagonal during the growth process to create heterostructure nanowires as shown in Fig. 2 of the main text. In particular, this is the result of the PbTe/(Pb,Sn)Te//Si(100) growth process. In the first part, the growth time of (Pb,Sn)Te was 120 min, while in the second part, we grew PbTe for only 10 min. However, Fig. 2 of the main text shows that the lengths of the two NW parts are comparable. The growth of PbTe was carried out by turning off the SnTe flux for initial (Pb,Sn)Te and the PbTe flux remained unchanged. This means that the growth rate in the PbTe part decreased 3 times, for this particular condition. The growth time was 12 times shorter. Hence, it suggests that both parts consist of (Pb,Sn)Te rather than PbTe/(Pb,Sn)Te. Further studies would be needed to establish the chemical composition of both parts of these NW heterostructures.

Appendix B: Computational details

Electronic structure calculations were performed within the framework of the first-principles density functional theory based on plane wave basis set and projector augmented wave method using VASP[2] package. The structural relaxations are performed without SOC, while all the band structure calculations of the main text are fully relativistic by considering SOC, a plane-wave energy cut-off of 250 eV has been used. As an exchange-correlation functional, the generalised gradient approximation of Perdrew, Burke, and Ernzerhof has been adopted[3]. We have performed the calculations using 1×1×12 k-points centered in Γ. The electronic band structures are computed with 60 k-points between the Γ and Z direction. The convergence criterion for the force is considered to be 0.01 eV/Å, while 10^{-5} eV of energy tolerance is taken for structural relaxation. In the high-symmetric structure, we study the systems without structural relaxation to study the system with perfect C_4 symmetry in the regions among the twinnings.

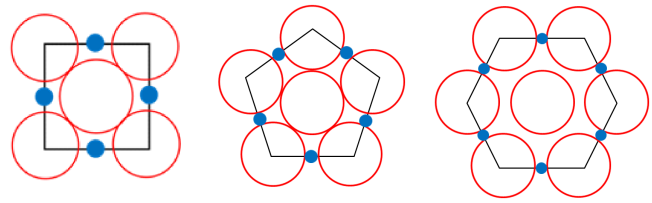

FIG. 1. Three types of polygon i.e. cubic, pentagon and hexagon are considered to calculate the particle density and Madelung constant. The atoms are represented by circles. The N red atoms on the vertices have a radius of R, while the N blue atoms on the sides of the polygons have a radius of r. The size of the blue and red atoms is defined to maximize the area occupied. This maximizes the density and atomic packing factor from a physical point of view; from a mathematical point of view this constraints a relation between r and R such that the density is only a function of one variable that we choose to be x equal to the ratio between the two radii.

Appendix C: Semiclassical approach to describe the stability of ionic pentagonal NWs

Since the pentagonal geometry is poorly studied, we also calculated some semiclassical quantities to unveil the reasons for its structural stability. For instance, the Madelung constant and the particle density for three types of polygons such as square, pentagon, and hexagon are calculated. Finally, we combine both the properties in one plot showing that the pentagonal NWs can be formed in case of an interplay between ionic and covalent bonds.

The three types of polygons considered are shown in Fig. 1. Two types of atoms with different atomic radii are studied and general equations for particle density in two dimensions (2D) are used. The atoms are positioned on the sides and corners of the polygon, the size of the side atoms (r) is variable and smaller than the corner atoms (R). Hence, two regions are studied i.e. $r<r_c$ and $r>r_c$. Here r_c is the critical value of the radius for which the side atom touches the corner one and the density becomes maximum. The general formula for the particle density D_N in the case of NWs with a polygonal section having N sides (N is 4, 5 and 6 for the square, pentagon and hexagon respectively) can be written as;

$$D_N = \frac{\text{Area of occupancy of atoms}}{\text{Total area of the Polygon with N sides}}$$

$$D_N(x) = \begin{cases} \frac{\pi}{4\sin(\frac{2\pi}{N})}\left(1+x^2\right) & \text{if } 0<x<x_c \\ \frac{\pi}{2}\tan(\frac{\pi}{N})\left(1-\frac{2x}{(1+x)^2}\right) & \text{if } x>x_c \end{cases} \quad \text{(C1)}$$

We define x=r/R where r is the radius of the side atoms and R is the radius for the atom at the corners. The particle density $D_N(x)$ reaches a maximum at a critical value

x=x$_c$ and afterward starts to decrease. We are interested in analyzing the dependence of the density $D_N(x)$ from the number N of sides of the polygon; the easiest way is to evaluate the density at x=0. In the square environment, the particle density is calculated to be 0.785 for x= 0 (r = 0), while it is increased to 0.919 if the radius of the atom located on the side of the polygon approaches the critical value x_c by touching the corner atoms. However, the density again decreases for $x > x_c$ and becomes 0.785 when $r = R$. An almost similar trend is followed by pentagons and hexagons. We want to focus on the dependence of the density from N that is in the coefficient and independent from x. Therefore, we evaluate the particle densities at $x = r = 0$ and report them in Table I. We got the highest density for the hexagonal structure, the lowest for the square, and the intermediate for the pentagon. The hexagonal structure possesses the highest particle density revealing that the covalent bond is favorable in this case, which means more covalent character pushes the system to stay in the hexagonal phase.

Polygon	Particle density	Madelung constant
Square	0.785	1.172
Pentagon	0.825	0.694
Hexagon	0.906	0.464

TABLE I. Particle density and Madelung constant calculated for the square, pentagonal, and hexagonal structures. We assume Q=d=1.

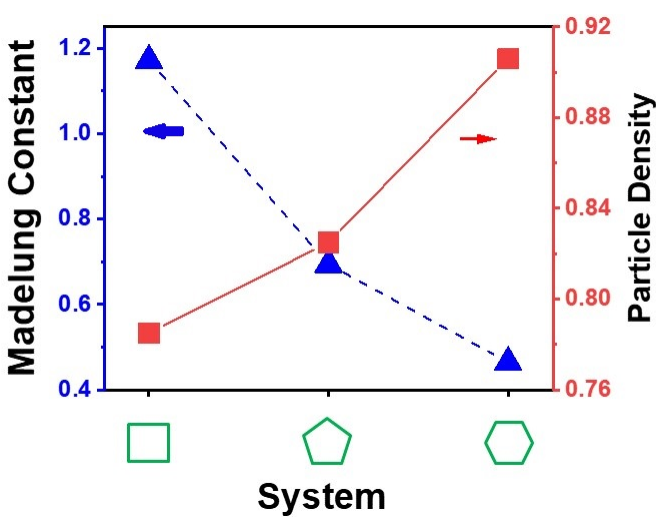

FIG. 2. Particle density (on the right y-axis, red) and Madelung constant (on the left y-axis, blue) calculated for the square, pentagonal, and hexagonal structures. The pentagonal structure bears the intermediate values for both the Madelung constant and particle density.

The Madelung constant determines the electrostatic potential for a single ion in a crystal by approximating the ions with point charges. The Madelung constant is a quantity typically referred to periodic lattices, in this case, it is meant to infer the electrostatic potential at the core center that would help to stabilize the formation of the NWs. We calculate the Madelung constant for square, pentagon, and hexagon. Generally, the Madelung constant is defined as:

$$M_N = \sum_j \frac{z_j}{r_{ij}}$$

where z_j is the number of j-th ions, r_{ij} is the distance between the ions with N= 4, 5, and 6 for the square, pentagonal, and hexagonal structures, respectively. Considering Q (opposite for the two atoms) as the charge and d as the distance between the two atoms, in the case of a square structure, we have:

$$M_4 = \frac{Q}{d}\left(4 - \frac{4}{\sqrt{2}}\right) = 1.172\frac{Q}{d}$$

In the case of a pentagonal structure:

$$M_5 = \frac{Q}{d}\left(\frac{5\sqrt{10-2\sqrt{5}}}{\sqrt{5}+1} - \frac{5\sqrt{10-2\sqrt{5}}}{4}\right) = 0.694\frac{Q}{d}$$

while for the hexagonal structure:

$$M_6 = \frac{Q}{d}\left(2\sqrt{3} - 3\right) = 0.464\frac{Q}{d}$$

The value of the Madelung constant is very crucial in the case of ionic bonds. As expected, we got the highest value of the Madelung constant for the square system (1.172) and the lowest (0.464) for the hexagon, while the pentagon bears the intermediate value (0.694). The large value of the Madelung constant for a square system indicates the highest contribution to ionicity and implies an ionic insulator scenario, which favors the system to be in the cubic structure.

For thick shells, most of the volume of the pentagonal NW will have the cubic arrangement so that the binding energy of the pentagonal NW will converge to the binding energy of the cubic structure as we observe from our results on the binding energy in the main text. For thick shells, the Madelung constant of the pentagonal structure will converge as well to the Madelung constant of the cubic structure for the same reasons. However, the Madelung constant for small thicknesses that we have calculated should be the relevant quantity in the formation of the disclination during the initial phase of the growth process.

This manifestation of the highest Madelung constant and lowest particle density for the square indicates the dominance of ionic character in the cubic structure, while the lowest Madelung constant and highest particle density for the hexagonal structure indicate that the system presents a more covalent character in this phase. On the other hand, intermediate values of Madelung

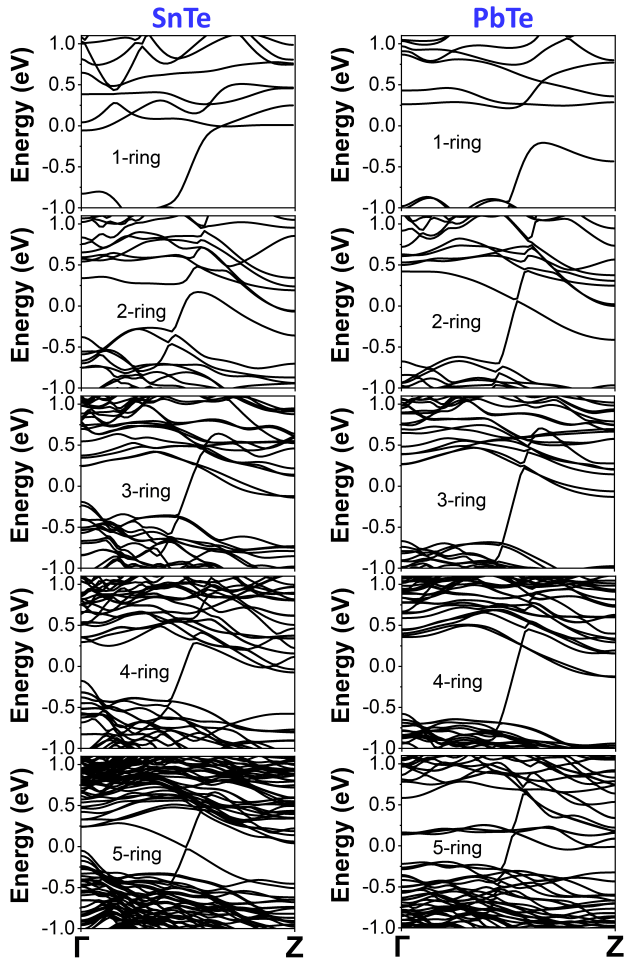

FIG. 3. Band structures of SnTe and PbTe pentagonal NWs in the $\Gamma - Z$ direction grown along [110] with cationic twin-boundaries without SOC. (Left panel) SnTe NWs, (right panel) PbTe NWs. One can see a band in most cases, which connects the valence and conduction electrons giving rise to metallicity. The Fermi level is set to zero.

constant and particle density for the pentagonal shape (see Fig. 2) reveal the contribution of both the ionic and covalent characters in the bond formation, which implies that if the bond is partially ionic and partially covalent, the pentagonal structure is expected to be the most stable. In the NWs based on lighter elements such as Se and Sn, the bonds would be more ionic, therefore we expect to be less likely to form a pentagonal crystal structure. Therefore, NWs based on Pb and Te would be more likely to form pentagonal NWs.

To summarize, from a semiclassical point of view, we understand that the interplay between covalent and ionic bonds favors the formation of pentagonal NWs. The quantum calculations reported in Section III of the main text demonstrated that the pentagonal NWs are metastable with the ground state being the cubic NWs. The difference between the ground state energies of cubic and pentagonal NWs becomes very small for thick NWs paving the way for the experimental formation of pentagonal NWs.

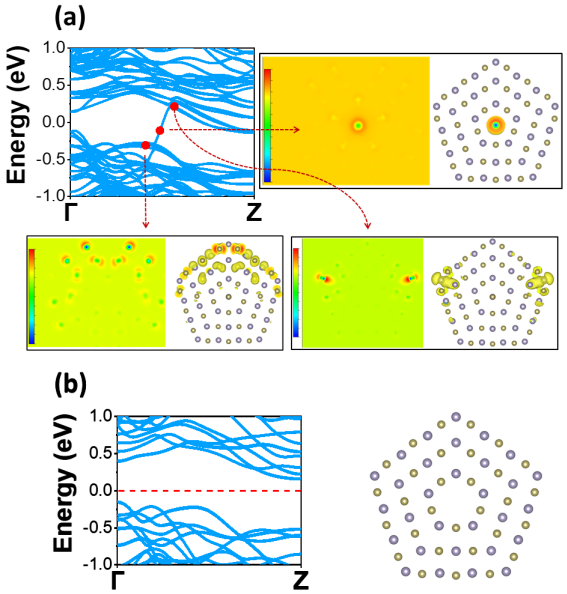

FIG. 4. (a) Band decomposed charge density obtained at different points along the $\Gamma - Z$ direction for the pentagonal NWs oriented in [110]. The charge density is distributed in the center of NW in real space when it is not hybridized (indicated by the red dot in the middle). (b) Band structure of the 3-ring pentagonal NW without the core chain, the band connecting the valence and conduction electrons disappears.

Appendix D: Band structure of the [110] pentagonal SnTe and PbTe NWs without SOC

In Fig. 3 we show the band structures of these systems without considering SOC interaction; here, both the compounds manifest bands that connect valence and conduction regions except 1-ring PbTe NW, which has an indirect band gap of 0.423 eV. The band connecting valence and conduction at the Γ point is in the conduction band and goes in the valence band increasing k as opposite to the pentagonal NW with [001] orientation. In Appendix E, we show that the core chain is responsible for the metallicity in the systems. Indeed, the band connecting the valence and conduction electrons disappears when the core chain of atoms is removed. Therefore, this band connecting valence and conduction is not related to topological properties since is not a surface band. This band, coming from the one-dimensional core chain, is composed of p_z orbitals of Sn and Te with a very short distance, therefore it would be very difficult to reproduce within the tight-binding models based on a bulk cubic environment with the normal lattice constant. The central atoms (a Sn and Te atom in the unit cell) have around 0.5 electrons more than other atoms, while

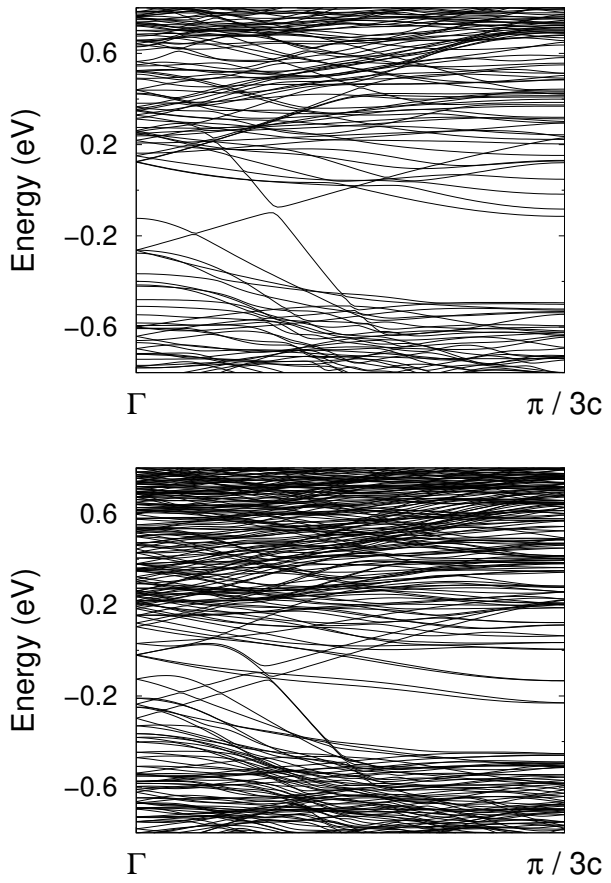

FIG. 5. Band structure for the optimized 5-ring pentagonal NW with Sn-twin boundary using ONETEP. The top panel is without SOC, while the bottom panel is with SOC. This figure should be compared with Fig. 5 of the main text.

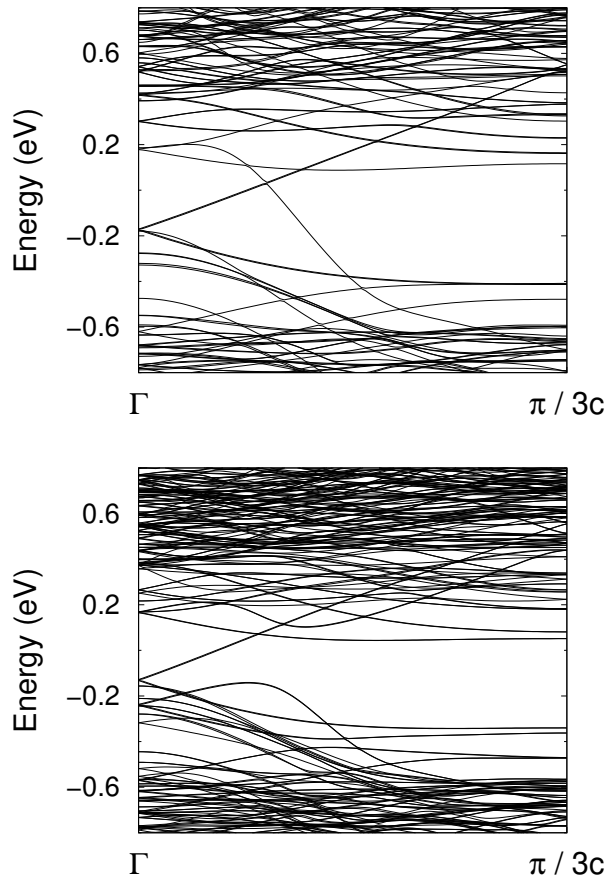

FIG. 6. Band structure for the optimized 5-ring pentagonal NW with Te-twin boundary using ONETEP. The top panel is without SOC, while the bottom panel is with SOC. This figure should be compared with Fig. 5 of the main text.

the first and second-ring atoms have a little less charge of around 0.01 electrons. These 0.5 electrons are due to the different structural environments of the CC or to the fractional charge.

Appendix E: Removing the core chain

Here, we calculate the band decomposed charge density at different k-points along the $\Gamma - Z$ direction for the SnTe pentagonal NWs oriented along [110]. To check the influence of the core chain on the electronic structure, we show the band decomposed charge density in Fig. 4. The charge density for the band connecting the valence and conduction sectors is distributed in the center of NW in real space when we consider a point in the middle of this band, namely not hybridized. Instead, when we take points where this band is hybridized with other electronic bands, the charge density is distributed in other regions as well, as shown in Fig. 4a). These results clearly indicate that the core chain is responsible for the metallicity in the systems. Further confirming this claim, we removed the core chain of the 3-ring pentagon (the remaining crystal structure is composed of only atoms in a NaCl-phase environment with 6 nearest neighbors) and calculated its band structure as illustrated in Fig. 4b). The band connecting the valence and conduction electrons disappears when the core chain of atoms is removed. The pentagonal SnTe NW without the core chain becomes a simple band insulator as expected for SnTe NWs with a cubic environment in the ultrathin limit. We observe the same behavior also for the [001] pentagonal NWs.

Appendix F: Reproducing the electronic structure within the ONETEP code

To double-check the results obtained within VASP, we perform electronic structure calculations with a DFT code that uses a different basis for the charge density as ONETEP[4,5]. The computational framework was presented in a previous paper[6]. The results are reported in Figs. 5 and 6 for the 5-rings optimized structure of

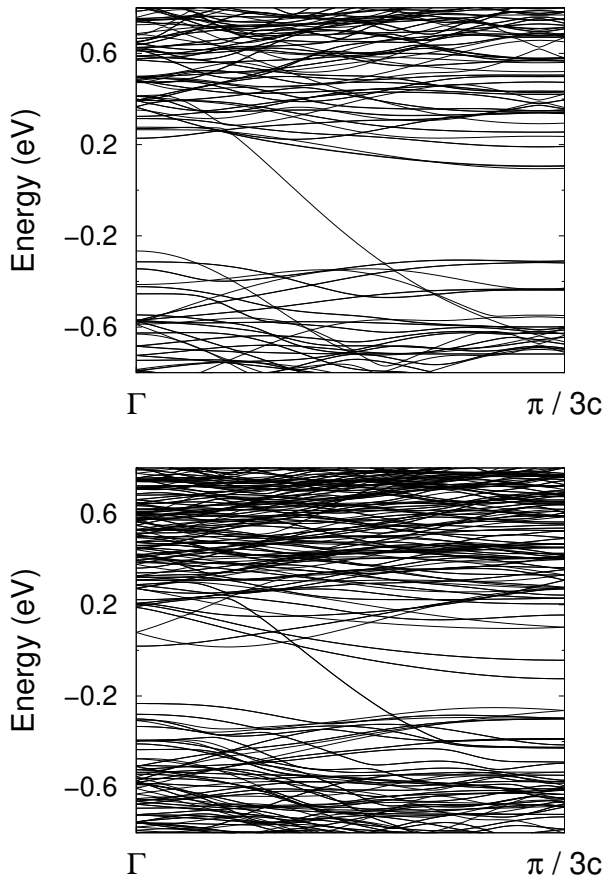

FIG. 7. Band structure for the high-symmetric 5-ring pentagonal NW with Sn-twin boundary using ONETEP. The top panel is without SOC, while the bottom panel is with SOC. This figure should be compared with Fig. 6 of the main text.

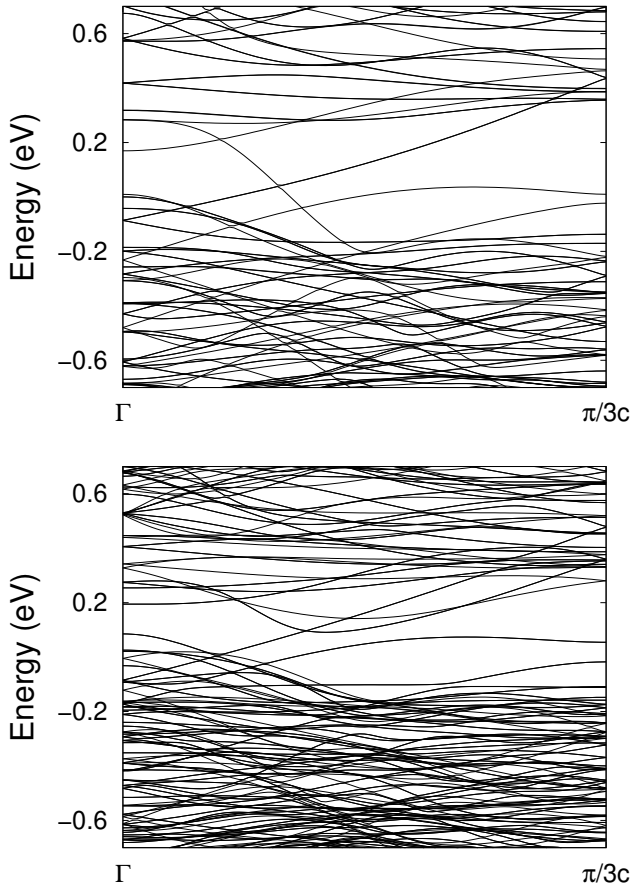

FIG. 8. Band structure for the high-symmetric 5-ring pentagonal NW with Te-twin boundary using ONETEP. The top panel is without SOC, while the bottom panel is with SOC. This figure should be compared with Fig. 7 of the main text.

SnTe with Sn and Te twin boundaries, respectively. The results for the 5-rings of SnTe with high-symmetry structure and with Sn and Te twin boundaries are reported in Figs. 7 and 8, respectively. In order to do this, we repeat the unit cell three times along the c-axis, this produces a triple downfolding of the band structure. Due to the downfolding, the metallic band has an opposite inclination with respect to the VASP but the results are strongly consistent with the VASP results. The SnTe band structures within ONETEP show a slightly larger gap for the shell bands as it happens in the cubic NWs[6].

Appendix G: Band structure under applied pressure

The study of the topological properties in the cubic NWs is extremely demanding computationally because of the thickness dependence of the topology. Indeed, we need to have a large thickness to reach the topological phase in the cubic NWs. In cubic bulk SnTe and PbTe compounds, the effect of the compression pushes the SnTe material-class compounds toward the topological region of the phase diagram. Since our thin NWs are extremely thin the cubic shell region is in a trivial regime, we apply compression in order to observe the topological transition in the shell region. The transition of the cubic shell from the trivial to the topological phase for the pentagonal NWs should go through a closure of the trivial band gap at one or both high-symmetry points Γ and Z. The effect of compression on the electronic band structures of symmetric 5-ring SnTe pentagonal NW with Te on the twin boundaries is shown in Fig. 9. We notice a reduction of the band gaps at Γ and Z, the systems become more metallic as the compression is increased due to the increasing of the bandwidth as happens in bulk phases[7], however, no closure of the gap at Γ or Z is observed. Even if the thickness is too thin to develop a topological phase in the cubic SnTe, we have the connection between valence and conduction due to the core chain persisting at every pressure.

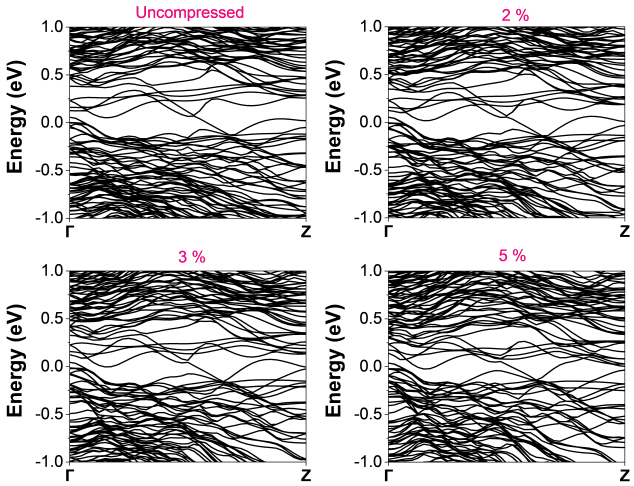

FIG. 9. Band structures of the high-symmetric 5-ring SnTe pentagonal NW with Te on the twin boundaries for the uncompressed and compressed systems. The calculations were performed with SOC. The Fermi level is set to zero.

Appendix H: Model Hamiltonian and its symmetries

Our starting model is composed of a p-orbital tight-binding Hamiltonian (p-orbitals for the cations and p-orbitals for the anions) described in the following formula:

$$\mathcal{H}(\mathbf{k}) = m\mathbb{1}_2\otimes\mathbb{1}_3\otimes\Sigma + t_{12}\sum_{\alpha=x,y,z}\mathbb{1}_2\otimes(\mathbb{1}_3 - L_\alpha^2)\otimes h_\alpha(k_\alpha) + t_{11}\sum_{\alpha\neq\beta}\mathbb{1}_2\otimes\left[\mathbb{1}_3 - \frac{1}{2}\left(L_\alpha + \epsilon_{\alpha\beta}L_\beta\right)^2\right]\otimes h_{\alpha,\beta}(k_\alpha,k_\beta)\Sigma + \sum_{\alpha=x,y,z}\lambda_\alpha\,\sigma_\alpha\otimes L_\alpha\otimes\mathbb{1}_8, \tag{H1}$$

which has been used for describing the bulk topological crystalline insulator phase in the SnTe materials[7] and various topological phases in lower dimensional systems[8,9]. Here we have chosen a cubic unit cell containing eight lattice sites, Σ is a diagonal 8×8 matrix with entries $\Sigma_{i,i} = \mp 1$ at the two sublattices (Sn and Te atoms), $\varepsilon_{\alpha\beta}$ is Levi-Civita symbol, $L_\alpha = -i\varepsilon_{\alpha\beta\gamma}$ are the 3×3 angular momentum $L = 1$ matrices, σ_α are Pauli matrices, and $h_\alpha(k_\alpha)$ and $h_{\alpha,\beta}(k_\alpha,k_\beta)$ are 8×8 matrices describing hopping between the nearest-neighbors and next-nearest-neighbor sites, respectively. In investigations of topological properties, it is useful to allow the spin-orbit coupling to be anisotropic, hence λ_α, although in this case, we have used $\lambda_\alpha \equiv \lambda$. For this paper, we have used numerical values that reproduce the band structure of SnTe which are $m = 1.65$ eV, $t_{12} = 0.9$ eV, $t_{11} = 0.5$ eV and $\lambda = 0.3$ eV.

* autieri@magtop.ifpan.edu.pl

[1] P. Dziawa, J. Sadowski, P. Dluzewski, E. Lusakowska, V. Domukhovski, B. Taliashvili, T. Wojciechowski, L. Baczewski, M. Bukala, M. Galicka, *et al.*, Crystal growth & design **10**, 109 (2010).

[2] G. Kresse and J. Furthmüller, Physical Review B **54**, 11169 (1996).

[3] J. P. Perdew, K. Burke, and M. Ernzerhof, Physical Review Letters **77**, 3865 (1996).

[4] C.-K. Skylaris, P. D. Haynes, A. A. Mostofi, and M. C. Payne, The Journal of Chemical Physics **122**, 084119 (2005), https://pubs.aip.org/aip/jcp/article-pdf/doi/10.1063/1.1839852/15362896/084119_1_online.pdf.

[5] J. C. A. Prentice, J. Aarons, J. C. Womack, A. E. A. Allen, L. Andrinopoulos, L. Anton, R. A. Bell, A. Bhandari, G. A. Bramley, R. J. Charlton, R. J. Clements, D. J. Cole, G. Constantinescu, F. Corsetti, S. M.-M. Dubois, K. K. B. Duff, J. M. Escartín, A. Greco, Q. Hill, L. P. Lee, E. Linscott, D. D. O'Regan, M. J. S. Phipps, L. E. Ratcliff, A. R. Serrano, E. W. Tait, G. Teobaldi, V. Vitale, N. Yeung, T. J. Zuehlsdorff, J. Dziedzic, P. D. Haynes, N. D. M. Hine, A. A. Mostofi, M. C. Payne, and C.-K. Skylaris, The Journal of Chemical Physics **152**, 174111 (2020), https://pubs.aip.org/aip/jcp/article-pdf/doi/10.1063/5.0004445/16741083/174111_1_online.pdf.

[6] G. Hussain, K. Warda, G. Cuono, and C. Autieri, ACS Applied Nano Materials **7**, 8044 (2024), https://doi.org/10.1021/acsanm.4c00506.

[7] T. H. Hsieh, H. Lin, J. Liu, W. Duan, A. Bansil, and L. Fu, Nature communications **3**, 1 (2012).

[8] P. Sessi, D. Di Sante, A. Szczerbakow, F. Glott, S. Wilfert, H. Shmidt, T. Bathon, P. Dziawa, M. Greiter, M. Neupert, M. Greiter, T. Neupert, G. Sangiovanni, T. Story, R. Thomale, and M. Bode, Science **354**, 1269 (2016).

[9] W. Brzezicki, M. M. Wysokiński, and T. Hyart, Phys. Rev. B **100**, 121107(R) (2019).